





Original Article

Enabling *In Situ* Studies of Metal-Organic Chemical Vapor Deposition in a Transmission Electron Microscope

Marcus Tornberg^{1,2,3} , Carina B. Maliakkal^{1,2,3} , Daniel Jacobsson^{1,2,3} , Reine Wallenberg^{1,2,3}  and Kimberly A. Dick^{1,2,3*} 

¹Centre for Analysis and Synthesis, Lund University, Box 124, 22100 Lund, Sweden; ²National Center for High Resolution Electron Microscopy (nCHREM), Lund University, 22100 Lund, Sweden and ³NanoLund, Lund University, 22100 Lund, Sweden

Abstract

The world of environmental microscopy provides the possibility to study and analyze transformations and reactions during realistic conditions to understand the processes better. We report on the design and development of a metal-organic chemical vapor deposition (MOCVD) system integrated with an environmental transmission electron microscope intended for real-time investigations of crystal growth. We demonstrate methods for achieving a wide range of precisely controlled concentrations of precursor gas at the sample, as well as for calibrating the sample partial pressure using the pressure measured elsewhere in the microscope column. The influences of elevated temperature and reactive gas within the pole-piece gap are evaluated with respect to imaging and spectroscopy. We show that X-ray energy-dispersive spectroscopy can be strongly affected by temperatures beyond 500°C, while the spatial resolution is largely unaffected by heat and microscope pressure for the relevant conditions. Finally, the influence of the electron beam on the investigated processes is discussed. With this work, we aim to provide crucial input in the development of advanced *in situ* electron microscopy systems for studies of complex reactions in real time under realistic conditions, for instance as used during formation of semiconductor crystals.

Key words: electron microscopy, energy-dispersive spectroscopy, environmental-TEM, *in situ*, instrumentation, MOCVD

(Received 14 January 2022; revised 11 March 2022; accepted 5 May 2022)

Introduction

Environmental transmission electron microscopy (ETEM) provides a powerful opportunity for studies within reactive environments, ranging from reduction, oxidation, and catalysis studies (Hansen et al., 2001; Toth et al., 2019) to structural transformations and crystal growth (Hashimoto et al., 1968; Hammar et al., 1996; Oh et al., 2005). In particular, the technique has evolved to enable real-time investigations at the atomic level under realistic conditions, ideal for detailed studies of crystal growth. Such studies benefit from precise control, monitoring, and variability of the ambient gas, potentially including multiple independently controlled species to which a sample is exposed at the same time. Earlier *in situ* studies of crystal growth have been conducted by supplying gas species using gate valves (Ross et al., 1998), Knudsen cells (Harmand et al., 2018), evaporation of solid materials mounted on the holder (Lenrick et al., 2014), or pre-mixing of a set volume of gas whose flow is controlled by mass flow controllers (Straubinger et al., 2017). The highly complex nature of the crystal growth process, however, means that

extrapolation of any findings to *ex situ* or industrially relevant processes requires increasingly higher accuracy and precision with respect to variability and quantification of gas pressures and compositions throughout the experiments. This represents a particular challenge for ETEM analysis and has required the design of systems that integrate the capabilities of advanced crystal growth instrumentation with the specific requirements of TEM to allow elevated sample pressure and temperature, as well as a better understanding how the environment influences the analysis and vice versa.

To address these challenges, we developed an ETEM system based on a Hitachi HF3300S instrument [reported in Hetherington et al. (2020)], which is integrated with a metal-organic chemical vapor deposition (MOCVD) system designed for real-time investigation of crystal growth processes of semiconductor nanostructures. Chemical vapor deposition is a well-established technique for crystal growth with broad application in the electronics industry, with MOCVD being especially important for synthesis of compound semiconductors. This method allows for the extremely accurate control of gas composition and pressure which is required to meet the very high demands on structural and chemical purity for modern electronic devices. However, this process typically operates at relatively high pressures (compared to TEM) in order to achieve the large-scale

*Corresponding author: Kimberly A. Dick, E-mail: kimberly.dick@ffl.th.se

Cite this article: Tornberg M, Maliakkal CB, Jacobsson D, Wallenberg R, Dick KA (2022) Enabling *In Situ* Studies of Metal-Organic Chemical Vapor Deposition in a Transmission Electron Microscope. *Microsc Microanal* 28, 1484–1492. doi:10.1017/S1431927622000769

© The Author(s), 2022. Published by Cambridge University Press on behalf of the Microscopy Society of America. This is an Open Access article, distributed under the terms of the Creative Commons Attribution-NonCommercial-NoDerivatives licence (<https://creativecommons.org/licenses/by-nc-nd/4.0/>), which permits non-commercial re-use, distribution, and reproduction in any medium, provided the original work is unaltered and is properly cited. The written permission of Cambridge University Press must be obtained for commercial re-use or in order to create a derivative work.

synthesis requirements. Moreover, the process requires the use of metal-organic and hydride precursor species with complex handling requirements, and for which calibration data is limited. Our research in MOCVD is focused on the use of this technique for synthesis of semiconductor nanostructures, such as nanowires, with interesting properties not otherwise achievable in conventional semiconductors. Since the properties of these materials are dependent on specific morphologies, structural, and compositional control achievable only in nanoscale processes, real-time investigation by ETEM is an ideal tool for understanding and controlling their synthesis.

Here, we demonstrate how the design of the ETEM-MOCVD instrumentation enables independent control of the gas composition and flow that reaches the heated sample region, as well as rapid adjustments of the gas supply. Previously, we briefly reported on the overall construction, technical specification, and capabilities of the system, with a primary focus on the TEM instrument (Hetherington et al., 2020). In the present work, we focus on the implemented solutions used for controlling gas concentration and pressures in the system and at the sample region. Solutions for calibration and monitoring partial pressures as well as total pressure in the microscope and at the sample are presented and evaluated, together with pressure correction factors of the pressure gauges for nitrogen (N_2), arsine (AsH_3), and phosphine (PH_3). In addition, we explore the influence that the temperature and gas supply to the microscope itself have on imaging and analysis, and conversely, how the imaging via electron beam influences the experiment. Effects of temperature and gas environment on spatial resolution are quantified, and we also demonstrate and quantify how X-ray energy-dispersive spectroscopy (EDS) analysis is influenced by the local reactive sample environment. Finally, the influence of the electron beam on the gas environment and on spectroscopic analysis is discussed.

Methods and Materials

The system described here is based on an image-corrected 300 keV cold-FEG equipped Hitachi HF3300S ETEM; detailed information of the TEM instrument and its capabilities are described in Hetherington et al. (2020). The standard microscope is modified with additional differential pumping using an additional aperture between the sample and the gun valve. This aperture creates an intermediate chamber between the objective pole-piece gap and the gun valve, which is supported by an additional ion pump to further increase the pressure difference between the sample region and the cold field-emission electron gun (cold-FEG). A visual representation of the microscope setup, including locations of pressure gauges and detectors, is presented in Supplementary material SI-1.

The ETEM is integrated with a custom chemical vapor deposition gas-handling system designed for use with metal-organic precursors as well as gas sources. The initial setup of the system is optimized for use with precursor species for III–V semiconductor growth, including trimethylgallium (TMGa), trimethylindium (TMIn), trimethylaluminum (TMAI), trimethylantimony (TMSb), arsine (AsH_3), phosphine (PH_3), hydrogen, nitrogen, and oxygen sources. However, the system can easily be modified for growth of other materials, taking advantage of its precision and flexibility of gas mixing, by changing the metal-organic or gas-phase precursors. Most of the experiments and calibration tests described in this paper are conducted using TMGa and AsH_3 (precursor sources for growing GaAs). The setup is

designed to operate with an open environment, often referred to as an open cell, which is evacuated using the constant pumping power of the microscope (Boyes & Gai, 1997). In turn, this allows for supply of multiple source gases in parallel, unrestricted access to a range of analysis techniques, holders with double tilt along with rapid replacement of gas concentrations. Gas flows and pressures are controlled by a series of mass flow controllers (MFC, HORIBA STEC Z500) and pressure transducers (PC, HORIBA STEC UR-Z71) between the source material and the microscope. Further details of the gas-handling apparatus are presented below together with the system design and calibrations of the gas species.

The system is additionally equipped with a mass spectrometer/residual gas analyzer (Stanford Research Systems RGA 300 amu) to quantify gas species after the sample, as well as an X-ray energy-dispersive spectrometer (Oxford Instruments XMax 80^N). Pressure calibrations and assessment of gas correction factors are determined using column pressure measured using magnetron Pirani gauges (Inficon MPG400) within the microscope as well as a gas invariant capacitance diaphragm pressure gauge (Inficon CDG045).

Experiments are conducted using specially designed microelectromechanical systems (MEMS) as heating chips. At present, two primary designs are used. The first type of chip, used for most of the results presented here, is provided by Norcada Inc. and consists of an electron transparent amorphous SiN_x film (Howe et al., 2017), which can be heated and operated to at least 700°C. Some chips of this type are also prepared with 2.3 μm diameter holes in the thin SiN_x , such that growing crystals can be imaged in vacuum. The second system is based on single-crystal silicon microcantilevers on which the same is grown directly (Kallesøe et al., 2010), allowing for a defined epitaxial relationship between the sample and the microcantilever.

Results

Design of an MOCVD-ETEM System for In Situ Experiments

The MOCVD system (Fig. 1) is designed with two primary gas lines connected directly to the microscope such that two different precursor species can be controllably supplied to the sample region without pre-mixing (which could otherwise lead to detrimental pre-reactions between, for instance, the group III and group V precursors). For liquid (and solid) metal-organic precursor species such as TMGa, H_2 is used as a carrier gas. A controlled flow of H_2 is bubbled through the metal-organic precursor bottle at a controlled temperature and pressure, so that the resulting gas mixture contains a known partial precursor flow. The fraction of precursor within the gas stream is determined by the ratio between the vapor pressure of the precursor and the pressure in the gas line (bubbler) and the absolute flow is scaled by the flow of carrier gas. The precursor concentration in the gas stream is continuously measured by the attached IR-300 vapor concentration measurement units (HORIBA STEC). In addition, the carrier gas flow through the bubbler is kept low to not alter the temperature of the precursor source due to the temperature difference between the carrier gas and the precursor source. As a result, we can rely on the controlled temperature of the bath in which the precursor bubbler rests to reflect the precursor temperature at these conditions. This particular gas-handling system can maintain a stable pressure between 5 and 200 kPa. Gas-phase sources, including the hydride precursors (AsH_3 and PH_3) as well as H_2 , N_2 , and O_2 , can be supplied directly using MFCs to control the

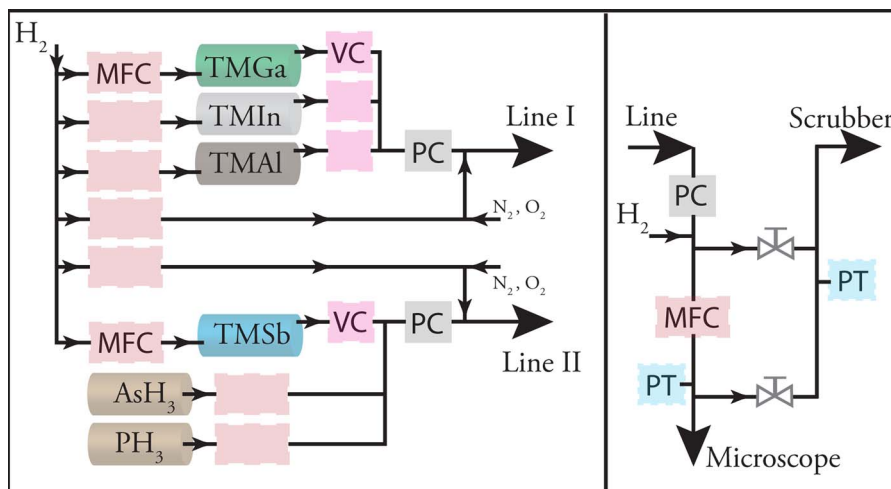


Fig. 1. Schematic of the (MOCVD) gas-handling system in Lund: The material flow is controllably supplied in two parallel gas lines to separate two primary reactants (here: group III and group V precursors). As for conventional MOCVD of III–V semiconductors, the H_2 can be used as both carrier gas, and a dilution source for the gas flow. The left schematic shows the design for deterministic gas mixing using mass flow controllers (MFCs), volume concentration measurements (VCs), and pressure controllers (PCs). After the pressure control, seen in both schematics, additional H_2 can be supplied for dilution before restricting the flow which is to be supplied to the microscope using an additional MFC. The gate valves that lead to the absorbing scrubber are used to by-pass material which are not supplied to the microscope.

flow. In addition to the extraction process, all precursor species can be further diluted with H_2 to obtain a wide range of volume concentrations of individual precursors within the gas stream. Furthermore, the gas-handling design allow for more than one precursor material to be mixed in the gas stream of each of the two separate gas lines at any given time, which improves flexibility of the constituents of the gas.

The design of the gas-handling system and particularly the ability to dilute the precursor species with additional high flow of H_2 allows for a very wide range of precursor flows and partial pressures to be achievable, spanning over four orders of magnitude (approximately 4×10^{-6} to 0.1 Pa of TMGa, or 7×10^{-5} to 2 Pa of AsH_3). For the purpose of crystal growth of binary semiconductors, this allows us to achieve flows/partial pressures that are comparable to conventional MOCVD growth of semiconducting nanostructures (Joyce et al., 2010; Lehmann et al., 2013; Wang et al., 2019). This allows us to directly compare the results achieved *in situ* with *ex situ* growth, and facilitates investigations of the effect of the electron beam on crystal growth.

Although the flows achievable in our system and the precursor partial pressures that can be achieved at the sample are comparable to conventional MOCVD growth, standard commercial reactors operate at much higher total pressure (typically within an order of magnitude of atmospheric pressure), mainly achieved by a high flow of H_2 (or N_2) carrier gas. Obviously, such high pressures are not suitable for electron microscopy unless the gas is completely isolated from the rest of the microscope, as in the case when using a closed environmental cell (Allard et al., 2012; Garza et al., 2017). As noted above, however, a closed cell limits resolution, sample tilt, spectroscopic analysis and gas switching time, among other things. To improve the compatibility of the gas control system and the microscope, we utilize an additional mass flow controller to reduce the gas flow provided to the microscope, bypassing excess flow directly to the absorber/scrubber, as can be seen in Figure 1. As a result, this can reduce the flow to the microscope, down to 0.1% of the total flow of the gas-handling system while still maintaining the relative gas concentrations.

For interfacing the gas-handling system and the microscope, we opted for two solutions: supplying gas via capillary tubes passing through the sample holder, or through side-port mounted nozzle injectors directly into the objective pole-piece gap. The former pathway is similar to closed environmental cells since the gases are supplied via capillary tubes through the holder, but without the need for outlet capillary tubes since the gases flow directly into the microscope. It requires the gas-handling system to be directly attached to the holder which may cause propagation of vibrations between the gas-handling system and the stage (in particular, stainless steel tubes as used in conventional MOCVD systems were found to translate a significant amount of vibration). To limit this transference, we bridged the gas-handling system and the holder using thin ($530 \mu m$ inner diameter) flexible polymer-coated (PolyEther Ether Ketone, PEEK) quartz capillary tubes. One benefit of supplying gas through the holder is the possibility to partially enclose the sample region to allow increased sample pressures. This is done by covering the sample region with a steel lid that has an orifice for the electron beam. It adds a differential pressure step from the sample region to the objective pole-piece gap by restricting the gas flow which in turn enables microscopy at sample pressures as up to 400 Pa, while still keeping the column pressure below 2 Pa. This can be considered a middle ground between the open environment and the closed cell design. Using this additional capillary tubing contributes to a pressure drop (3–4 orders of magnitude) between the gas-handling system and the holder, which provides an inherent delay in gas switching. As a result, changes of the gas concentration or flow can require up to a few minutes to reach a time invariant pressure within the microscope column. Such a delay can be detrimental to studies that depend on rapid gas flow changes, but is nevertheless on par if not faster than the reported delay in closed cell experiments (Tan et al., 2019).

Our second approach for providing gas to the sample region, through a nozzle injector connected to a microscope side-port, delivers the gas directly to the microscope chamber without passing through the holder. This approach provides a separation between the holder and the gas supply, where the gas is provided

from a stationary point at an angle above the sample holder itself. As a result, the length of the capillary tubing can be greatly reduced in comparison to when supplying through the holder, and thus reduces the pressure difference between the gas-handling system and the sample. Consequently, changes in material flow results in stabilization of partial pressures at the sample within typically 30 s, depending on the absolute pressure and if the flow is increased or decreased. The pressure data as a function of gas flow change is illustrated and provided in Supplementary material SI-2.

The two designs come with their own advantages. Supplying material through the holder allows for experimental conditions invariant to sample tilt, as the gas outlet moves with the holder along with the possibility of adding a lid to increase the sample pressure. Furthermore, it is less sensitive to fluctuations in gas flow due to the relatively longer time needed to stabilize pressure after flow changes. In contrast, supplying gas to the pole-piece gap via the nozzle injector allows simpler design of holders with double tilt possibilities, faster environment adjustments and a lower sensitivity to vibrations due to not having the gas-handling system connected to the holder.

Calibration and Evaluation of the Microscope Environment

To evaluate the environment within the microscope, we probe the gas flow and pressure both up- and downstream from the sample region as well as at the sample. We control and continuously monitor the upstream gas composition and flow using the designed gas-handling system presented in Figure 1 and the gas supplied to the sample is regulated by mass flow controllers and monitored using pressure transducers. To monitor and observe the environment at the sample and downstream toward the turbo pump acting on the pole-piece gap, we utilize the pressure calibrations based on the column pressure and mass spectrometry (residual gas analysis), respectively.

Gas analysis downstream from the sample holder using the residual gas analyser (RGA) does not directly reflect the gas composition at the sample region. This is due to that we have observed a lack of change in the RGA response as a result of increasing the sample temperature beyond onset of precursor decomposition. This may be a result if the change in gas composition is minor in comparison to the gas interaction with the heated RGA filament or that the interaction volume at the sample is small in comparison to the flux. However, the RGA responds readily to

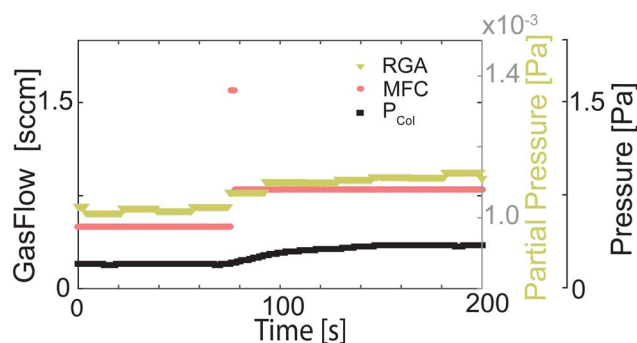


Fig. 2. Monitoring the response time of the column pressure and the residual gas analyzer with respect to the flow changes. An instant change of gas flow (MFC) from the gas-handling system provides the pressure buildup within the microscope. A larger dataset is presented in Supplementary material SI-2.

changes within the material flow, as seen for AsH_3 in Figure 2. The residual gas analyzer thus complements the pressure measurement in the cases where the gas stream composition is changed; more than one species is supplied through the same gas line; or when the material is bypassed to the absorber after the final mass flow controller of the gas-handling system. However, we observe that it takes up to a minute for the pressure to stabilize even if the mass flow stabilizes instantaneously. When supplying more than one gas, we observe a co-dependence on the measured partial pressures by the RGA when altering the influx of one of the species. Although the dependence might not always be monotone, as can be seen in Supplementary material SI-2, it can be accounted for by calibrating the signal to a constant flow for the individual species (Maliakkal et al., 2019).

Calibration of the Sample Partial Pressure

In contrast to a conventional MOCVD system, an ETEM-MOCVD operates at constant pumping power rather than at constant pressure, which makes the measurement of the sample pressure non-trivial. To evaluate the sample environment, we utilize gas-dependent pressure gauges (calibrated in air) of the microscope column to calibrate the pressure in the sample region. In addition, since the pressure readouts are gas-dependent, we determine the pressure correction factors of the pressure gauges for each individual species.

The calibration between the sample pressure and the microscope column pressure was performed in two steps. First, we use a MEMS device, normally used for heating of a SiN_x membrane (Howe et al., 2017), as a pulsed Pirani gauge for measuring the resistance through the heating coil (i.e., the temperature) at constant biasing. This is used to correlate the measured bias of the MEMS for known pressure for a set of resistances (temperatures), which were in turn measured in a closed *ex situ* environment as the one described in Hetherington et al. (2020). This initial correlation is then used to evaluate the cooling effect of a gas flow. Second, once the cooling behavior is known, we utilize this behavior to calibrate the sample pressure with respect to the microscope column pressure. In determining the sample pressure, we assume it to be homogeneous across the sample region, which is based on the measured pressure differences being less than 5% within the region of interest.

For the specific case of supplying gas through the holder, only one calibration was needed since the gas flow is fixed with respect to the holder. This provided a sample calibration factor of 2 with respect to the microscope pressure (i.e., sample pressure is determined to be approximately twice the microscope pressure). The higher pressure at the sample is a consequence of the sample being placed much closer to the gas supply (approximately 3 mm) than the microscope pressure gauge.

For gas supplied through the nozzle injector via the side-port of the microscope, sample pressure is also dependent on tilt, since this changes the distance between the sample and nozzles. Pressure calibration in this case was therefore performed using discrete measurements at intervals of 2.5° (α) and 3° (β), starting from the origin (0, 0), for the stationary nozzle injector. The calibration of sample pressure for each orientation of the sample and for each gas inlet is shown as color maps in Figure 3. The changes in gas pressure at the sample can then be correlated with the physical positioning of the inlets with respect to the holder. These calibrations allow for more representative measurement of the ambient where the reaction is taking place along with the

feedback on the relative positions and orientations of the two gas inlets.

To find the partial pressures at the sample from the pressure calibration presented above, we determined the pressure correction factors for the gas species of interest (AsH_3 , PH_3 , and N_2). By parallel pressure measurements using magnetron Pirani gauge (Inficon MPG400) of the microscope and a gas-independent pressure gauge (capacitance diaphragm gauge, Inficon CDG045), we could directly correlate the pressure readouts shown in Figure 3. From the correlation, we extracted the individual correction factors (CFs) from the derivative (i.e., linear fit) of the pressure readings defined according to

$$\text{CF} = \frac{\partial p_{\text{CDG}}}{\partial p_{\text{MPG}}}$$

In this case, we determine the uniform correction factor over the pressure range for N_2 as 1.2, based on the data as presented in black in Figure 4. Using the experimental data presented for AsH_3 (gray) and PH_3 (magenta) we determined the gas correction factors for pressures between 0.001 and 10 Pa, which is the attainable pressure range within the microscope during for crystal growth (Maliakkal et al., 2019; Tornberg et al., 2020; Persson et al., 2021). As a result of the MPG400 being a dual pressure gauge, we extracted correction factors for both the cold-cathode filament (<0.06 Pa) and the Pirani element (1–10 Pa). Calibrations factors for PH_3 were found to be 2.487 ± 0.003 for the cold-cathode pressure range and 2.265 ± 0.038 for the Pirani range, while for AsH_3 the calibration factors were found to be 2.665 ± 0.003 for cold-cathode and 0.861 ± 0.047 for Pirani pressure ranges. Worth noting is that the extracted correction factor of PH_3 compares well with the reported value for ionization vacuum gauges (Instruments, 2021). For completion, since we use H_2 as a carrier gas, the gas correction factor of H_2 (2.4 for cold-cathode and 0.5 for Pirani) has been provided as a reference from the manufacturer (Inficon, 2006). This reference calibration is used in place of a calibration of the metal-organic sources to determine the partial pressure of the

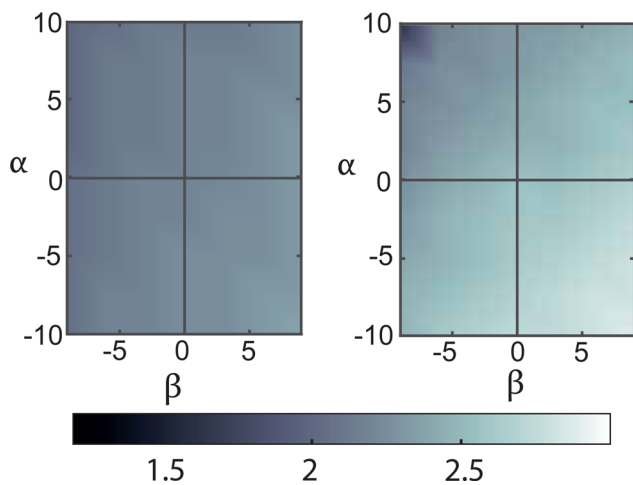


Fig. 3. Stage tilt-dependent calibration factors correlating the sample pressure of N_2 with respect to the column pressure which is obtainable during experiments for gas-injectors dedicated to group III (left) and group V (right) elements. The resulting color map are interpolated from the discrete measurements at intervals of 2.5° (α) and 3° (β) starting from the origin (0, 0). The mesh used for data-interpolation corresponds to the tilt accuracy of the stage, and the non-interpolated data is supplied in Supplementary material SI-3.

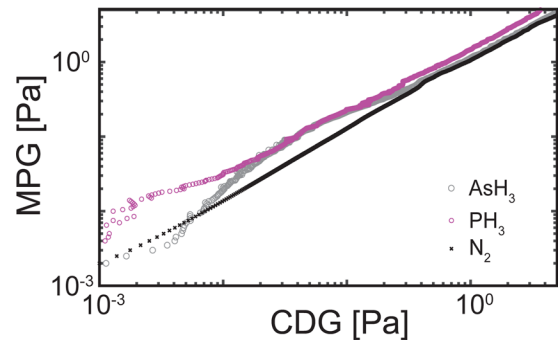


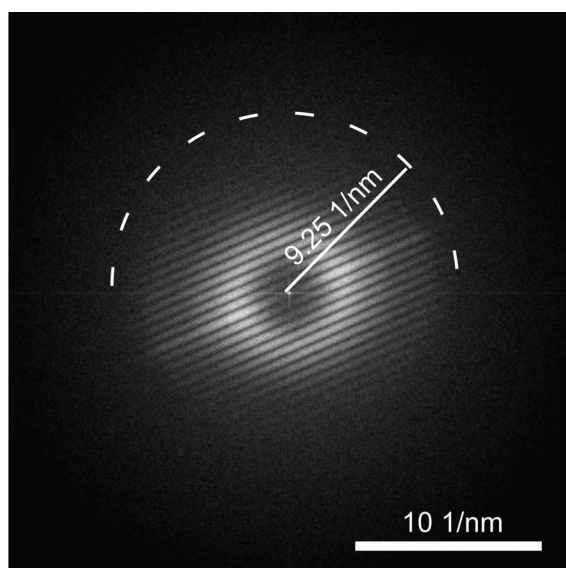
Fig. 4. Correlation between pressure measurements using an inverted magnetron Pirani (MPG) and a capacitance diaphragm gauge (CDG). It is shown for N_2 , AsH_3 , and PH_3 whose correction factors were extracted using linear regression for both the intervals of the cold-cathode and Pirani element of the MPG.

metal-organic species at the sample. This is assumed to hold for typical low gas stream concentrations of the precursors (0–5%) where we can neglect the precursor contribution to the total pressure.

Effect of Heating and Reactive Environment on Spatial Resolution

The introduction of a region with elevated pressure by the sample may influence the imaging, in particular the achievable spatial resolution. Direct heating of the sample region may also introduce a small amount of sample drift that could limit achievable resolution. To determine the resolution limits during *in situ* experiments, we evaluate the spatial resolution of conventional TEM imaging using the sample holder and MEMS chips, with varied pressure and temperature. The spatial resolution is evaluated in frequency space using Young's fringes that arises from image shift during exposure of the SiN_x membrane. The resulting pattern (fast-Fourier transform) of the image is used to evaluate the information limit based on the vanishing fringes (Kisielowski et al., 2008). This method is used to compare the information limit for both types of connections between the gas-handling system and the microscope in vacuum (<0.001 Pa), at high temperature and at elevated pressure of nitrogen (1 Pa), all while having the gas-handling system in operation. The gas-handling system itself may introduce vibrations that additionally limit the resolution; by keeping the system in operation through this experiment, we aim to separate temperature and pressure effects from these purely instrumental effects. We emphasize that the values obtained here do not represent the maximum achievable resolution of the microscope under optimized conditions [0.86 Å, as discussed in Hetherington et al. (2020)].

A typical interference pattern (fast-Fourier transform of the recorded image of amorphous SiN_x film) is shown in Figure 5. The figure includes the maximum achieved resolution for different combinations of temperature and column pressures while supplying the gas through the holder or via side-port injector. From the figure, we observe some vibrations along the vertical axis which stems from a slight instability around the rotational axis of the holder. We see that in both cases the measured resolution is slightly worse than the 0.86 Å achieved under optimized conditions (measured in vacuum using a single tilt holder, conventional carbon grid, full intensity from the cold-FEG, and the



| P_{col} | Temperature | d_{Holder} | d_{SidePort} |
|------------------|-------------|---------------------|-----------------------|
| 10^{-3} Pa | 20 °C | 1.09 Å | 1.02 Å |
| 10^{-3} Pa | 200 °C | 1.10 Å | 1.04 Å |
| 1 Pa | 200 °C | 1.09 Å | 1.03 Å |
| 1 Pa | 600 °C | 1.10 Å | 1.07 Å |

Fig. 5. A typical example of how the fast-Fourier transform appears for a image taken of a SiN_x film when the image is frequently shifted using projection lenses. The transform presented are taken at a sample temperature of 600 °C and a column pressure of 1 Pa, which were reached by supplying N_2 through the side-port injector. The table presents the resulting maximum information limit reached during gas-handling operation. Further details on the dataset are provided in Supplementary material SI-4.

gas-handling system turned off). Supplying gas through the holder also results in marginally lower resolution than the side-port injectors. However, the reductions are relatively modest, and for instance sufficient for atomically resolved GaAs along the [110] axis. Most importantly, we can see that the effect of heating (up to 600 °C) and gas pressure (up to 1 Pa) are negligible for both material pathways. Further details and measurements on the spatial resolution and the beam intensity as a result of having a relatively high pressure are presented in Supplementary material SI-4.

Effect of the Sample Heating on X-ray Characterization

One advantage of using an open sample environment is that it simplifies the acquisition and interpretation of X-ray spectra during *in situ* experiments. The small, heated area of MEMS-based sample chips is also important to minimize thermal emission. X-ray characterization at elevated temperatures has been reported to exhibit energy broadening of elemental peaks (Kamino et al., 1997) and occasionally shifts of the detected signal to higher energies (pile-up) (Eswaramoorthy et al., 2007). The severity of these possible effects seems to vary with the design of the instrumentation (Kamino et al., 1997; Prestat et al., 2015; Omme et al., 2018). Of the two issues, the possible energy shift of elemental peaks would potentially be the most detrimental for an experiment

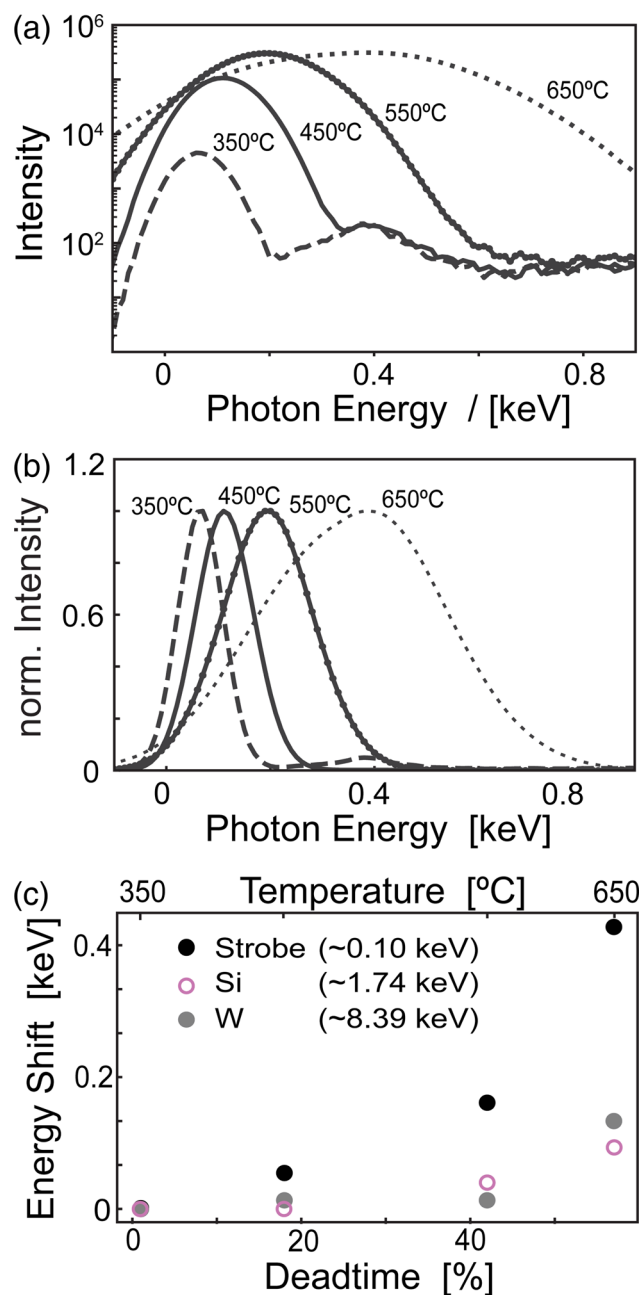


Fig. 6. The raw (a) and normalized (b) X-ray signal of the strobe peak is presented as a function of temperature. Note how the increased temperature results in an increased intensity and energy shift of the strobe peak for temperatures above 500 °C. The relative energy shift of elemental peaks (c) are presented as a function of temperature and the corresponding dead-time of the detector. Note how the elemental peaks of silicon and tungsten are less affected by the increased dead-time than the strobe peak.

since this would skew the quantification results significantly. Thermal energy broadening maintains the peak center of the elemental X-ray line, whereas an energy shift would, in the worst case, shift the entire peak away from the X-ray line (Kamino et al., 1997). Consequently, we evaluated the X-ray signal as a function of temperature for our specific chamber geometry.

For the SiN_x membrane MEMS devices, we observe that increasing temperature increases the thermal radiation and thus reduces the signal-to-noise ratio of the X-ray spectrum (Fig. 6a).

This appears as an increase in the total intensity of the spectrum (or dead-time of the detector) with temperature of two orders of magnitude over the temperature range evaluated, and results in both energy broadening and shift of the signal for specific temperatures. The temperature effect on the strobe signal is presented in Figure 6b displaying the shift occurring from 400°C.

The temperature effect observed here is not detrimental for quantification of elemental peaks (>1.74 keV) until reaching temperatures beyond 500°C as can be seen from Figure 6c, where the energy shift relative to the elemental line is shown for silicon and tungsten. Since the shift's origin is high intensity, it can be counteracted by reducing the signal reaching the detector, either by reduction of the solid angle or by controlling the X-ray sampling. The influence of solid angle (by retracting the detector) and signal intensity is presented in Supplementary material SI-5. In addition, the severity of this effect may also be limited by reducing the heated area, as a smaller heated region would in turn generate fewer photons related to the heating and thus lower the total intensity of the spectrum.

Interaction of the Electron Beam with the Reactive Gases

We next consider the effect of the high-energy electron beam on the reactive molecules within the gas. We anticipate some degree of beam-gas interaction, although the extent may be limited by the relatively small interaction volume. Since the system is equipped with a residual gas analyzer (RGA) for measuring the chemical composition of the gas after it has passed through the sample region of the microscope, we measured the effect on the RGA spectrum of different electron beam doses. The results shown in Figure 7a show no effect on the measured signal even at very high electron beam fluxes. This indicates that the fraction of the gas that interacts with the electron beam is very small, and not visible compared to the much larger signal from the gas that does not interact with the beam. Note that the highest electron

flux used in this experiment is the highest possible flux achievable in the microscope (with condenser aperture removed) and therefore an order of magnitude higher than would be used in a crystal growth experiment.

In addition, it is possible to investigate the effect of the electron beam on the reactive gas using X-ray energy-dispersive spectroscopy. This method is more suitable for detecting small effects, since we only see a signal from atoms that have interacted with the beam, and the effect is therefore not “drowned out” by the much larger volume of unreacted gas. For this, we quantified the signal that reaches the mounted XMax 80^N detector (Oxford Instruments) shielded by a polymer-based Moxtek window, that normally is operated before, during and after *in situ* experiments. By collecting X-ray signal from the illuminated gas-phase inside the pole-piece gap, without the presence of a sample or holder, we observe elemental peaks that correspond to the supplied precursors (in this case Ga from TMGa and As from AsH₃). Figure 7 shows how the signal from the scales with both pressure (source flow) and total beam flux (electrons/s), indicating that there is some interaction with the gas molecules and the electron beam. On the other hand, this does not tell us whether the ionization by the electron beam affects the decomposition of the molecules or the reactions that occur when they reach the sample.

It is also important to note that while we observe elemental information from the gas-phase, the magnitude of the signal is much smaller than that originating from the sample of interest. We also show in Figure 7b the signal from a 200-nm thick GaAs crystal acquired at low pressures (<0.001 Pa), with an electron flux of $1.37 \times 10^{11} \text{ s}^{-1}$ (open circles). The relative signal from gas (AsH₃ or TMGa) with respect to the sample at comparable flow rates is less than 0.1%. Consequently, the gas-phase contribution to the X-ray spectroscopy is negligible for elemental analysis of the sample. Note that the electron doses are presented as total electrons per second rather than per areal unit as we are mainly interested by the interaction with the gas and not the area of a sample.

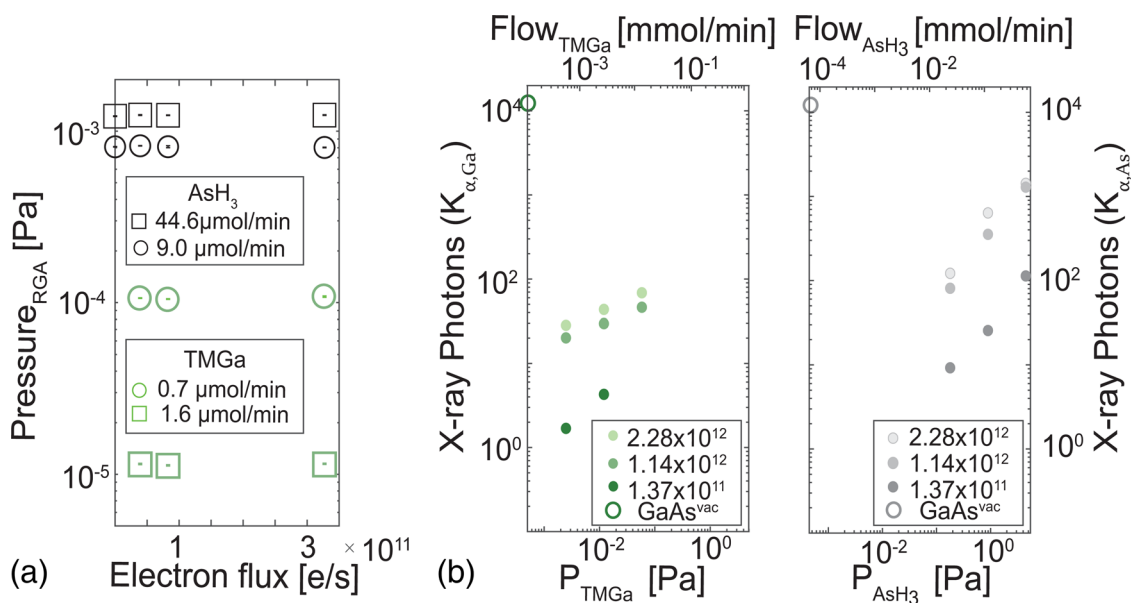


Fig. 7. (a) Partial pressure measurements at increasing electron fluxes tracking atomic masses of 78 and 101 atomic units for AsH₃ and TMGa, respectively. Note how the partial pressure are invariant to the electron flux as shown for two gas flows of each precursor. (b,c) The maximum peak intensity of the K_α peaks for gallium and arsenic as a function of partial pressure at the sample region (P) of the individual species for three electron fluxes. The data presented are acquired without any holder inserted to eliminate effects of the holder. For reference, the K_α signal of Gallium and Arsenic of a GaAs crystal in vacuum yields more than 100 times more photons detected at electron flux of 1.37×10^{11} electrons/s.

We also note that the total gas-generated X-rays are comparable between the individual gases but are scaled by the partial pressure (or molar flow). It is also worth noting that the TMGa flows used in this experiment are significantly (more than 5 times) higher compared to those used during a typical crystal growth experiment within our system (Maliakkal et al., 2019; Tornberg et al., 2020).

Beam Effect on Chemical Reactions

For any type of *in situ* experiments, it is of high interest to understand whether and how the measurement techniques affect the process of interest. For *in situ* experiments in TEM, the high-energy electron beam can affect the sample and chemical reactions in many ways, requiring a thorough analysis of the effects for the system of interest. Electron beam interaction and the electron dose-rate is well-understood to play an important role (Ek et al., 2016; Mirsaidov et al., 2020), as also shown above for EDS analysis, and many effects can be avoided by minimizing beam dose. However, well-understood and reproducible beam effects are not necessarily detrimental if they can be properly accounted for.

For a complex process like the semiconductor crystal growth experiments conducted in our system, a full understanding of the effects of the electron beam is very challenging, and will continue to be assessed for many years. Since we observed that the electron beam interacts with the precursor gas molecules, we first conduct a simple experiment to determine whether this affects the growth rate of GaAs crystals (which would be the case if the electron beam significantly changed the decomposition process of the precursors). Using GaAs nanowires as a model system, we evaluated the crystal growth rate (nm/min) both with and without illumination by the electron beam. For the dark experiments (conducted first, before the gas had been exposed to the electron beam for a significant time), we acquired a sequence of snapshots just before and after the gun valve had been closed/opened in order to measure the change in length during the “dark” period. For comparison, we next measured the growth rate by imaging in real time while exposing the sample to an electron dose-rate of 500–5000 e/Å² s. For these relatively low electron doses (typical for crystal growth experiments), there is no significant difference in growth rate (5.6 ± 1.2 nm/min under illumination versus 5.55 ± 1.2 nm/min without beam).

Although we do not observe significant effects for these experiments, there are a variety of possible ways that the electron beam can affect experiments, particularly at high doses. As such, it is necessary to carefully consider beam effects for each new type of material and process. As an extreme example, we have observed that imaging a GaAs nanowire at extremely high electron dose-rates (43,500 e/Å² s) while performing crystal growth at low partial pressure of TMGa ($<4 \times 10^{-4}$ Pa) can result in a change in the density of stacking defects occurring during the growth. Although this observation is at present anecdotal, and we cannot yet deduce the mechanism, it highlights the need to further study these effects for different processing and imaging conditions.

Summary

We describe here the design of a custom system integrating an aberration-corrected environmental TEM with an MOCVD system designed for investigating crystal growth of semiconductor materials in real time. The system is designed with an open holder to facilitate a wider range of sample tilt, access to complementary analysis techniques and faster switching of process gases. The

gas-handling system is designed for controlled experiments that mimic conventional MOCVD conditions as closely as possible, for instance including two separate gas lines that do not mix before reaching the sample. It is also designed to be flexible, allowing for a broad range of gas pressures and flows, and relatively easy changes of precursor types for studying a variety of different materials or different types of reactive processes. We demonstrate the solutions used to determine pressure around the sample regions and determine the gas correction factors for the AsH₃ and PH₃. We also evaluate the effects of the imaging and analysis on the experiments, and conversely how the experimental conditions (temperature and pressure) affect imaging and analysis. No effect of heating or gas pressure on spatial resolution is observed, and interaction of the electron beam with the gas is found to be small. For typical crystal growth conditions, we also do not observe a significant effect of the electron beam on the crystal growth rate. Potential effects of the electron beam on complex reactive processes are however numerous, and a full understanding of how the electron beam influences each process of interest will be a topic for continued study.

Supplementary material. To view supplementary material for this article, please visit <https://doi.org/10.1017/S1431927622000769>.

Acknowledgments. The authors acknowledge financial support from the Knut and Alice Wallenberg Foundation (KAW), NanoLund, and the Swedish Research Council (VR). We acknowledge Hitachi High-Technologies Canada and Europe and CollabraTech Solutions LLV for their contribution to the development and assembly of the instrument. We also acknowledge Inficon for their contribution to the process of determining pressure calibration factors. Lastly, we acknowledge Dr. Sebastian Lehmann for his contribution to the initial design and continuous discussions.

Competing interests. The authors have no conflicts of interest to declare.

References

- Allard LF, Overbury SH, Bigelow WC, Katz MB, Nackashi DP & Damiano J (2012). Novel MEMS-based gas-cell/heating specimen holder provides advanced imaging capabilities for in situ reaction studies. *Microsc Microanal* **18**, 656–666.
- Boyes ED & Gai PL (1997). Environmental high resolution electron microscopy and applications to chemical science. *Ultramicroscopy* **67**, 219–232.
- Ek M, Jespersen SP, Damsgaard CD & Helveg S (2016). On the role of the gas environment, electron-dose-rate, and sample on the image resolution in transmission electron microscopy. *Adv Struct Chem Imaging* **2**, 4.
- Eswaramoorthy SK, Howe JM & Phillipp F (2007). Microscopy microanalysis a shield for reducing the thermal signal from heating holders during in situ energy-dispersive X-ray spectroscopy analysis. *Microsc Microanal* **13**, 291–295.
- Garza HHP, Morsink D, Xu J, Sholkina M, Pivak Y, Pen M, Van Weperen S & Xu Q (2017). MEMS-based nanoreactor for in situ analysis of solid-gas interactions inside the transmission electron microscope. *Micro Nano Lett* **12**, 69–75.
- Hammar M, LeGoues FK, Tersoff J, Reuter MC & Tromp RM (1996). In situ ultrahigh vacuum transmission electron microscopy studies of heteroepitaxial growth I. Si(001)/Ge. *Surf Sci* **349**, 129–144.
- Hansen TW, Wagner JB, Hansen PL, Dahl S, Topsoe H & Jacobsen CJH (2001). Atomic-resolution in situ transmission electron microscopy of a promoter of a heterogeneous catalyst. *Science* **294**, 1508–1510.
- Harmand JC, Patriarche G, Glas F, Panciera F, Florea I, Maurice JL, Travers L & Ollivier Y (2018). Atomic step flow on a nanofacet. *Phys Rev Lett* **121**, 166101. doi:10.1103/PhysRevLett.121.166101
- Hashimoto H, Naiki T, Eto T & Fujiwara K (1968). High temperature gas reaction specimen chamber for an electron microscope. *Jpn J Appl Phys* **7**, 946–952.

- Hetherington C, Jacobsson D, Dick KA & Wallenberg LR (2020). In situ metal-organic chemical vapour deposition growth of III-V semiconductor nanowires in the Lund environmental transmission electron microscope. *Semicond Sci Technol* **35**, 034004.
- Howe JY, Thompson MS, Dogel S, Ueda K, Matsumoto T, Kikuchi H, Reynolds M, Hossainkhannazer H & Zega TJ (2017). In situ thermal shock of lunar and planetary materials using a newly developed MEMS heating holder in a STEM/SEM. *Microsc Microanal* **23**, 66–67.
- Ificon (2006). Operating manual: Inverted magnetron Pirani gauge MPG400-401 (tina48e1-c (2017-10) 1).
- Instruments M (2021). Technical resource: Gas correction factors for ionization vacuum gauges. Available at <https://www.mksinst.com/n/gas-correction-factors-for-ionization-vacuum-gauges>.
- Joyce HJ, Wong-Leung J, Gao Q, Tan HH & Jagadish C (2010). Phase perfection in Zinc Blende and Wurtzite III-V nanowires using basic growth parameters. *Nano Lett* **10**, 908. doi:10.1021/nl903688v
- Kallesoe C, Wen CY, Mølhave K, Bøggild P & Ross FM (2010). Measurement of local Si-nanowire growth kinetics using in situ transmission electron microscopy of heated cantilevers. *Small* **6**, 2058–2064.
- Kamino T, Sasaki K & Saka H (1997). High resolution electron microscopy in situ observation of dynamic behavior of grain boundaries and interfaces at very high temperatures. *Microsc Microanal* **3**, 393–408.
- Kisielowski C, Freitag B, Bischoff M, Van Lin H, Lazar S, Knippels G, Tiemeijer P, Van Der Stam M, Von Harrach S, Stekelenburg M, Haider M, Uhlemann S, Müller H, Hartel P, Kabius B, Miller D, Petrov I, Olson EA, Donchev T, Kenik EA, Lupini AR, Bentley J, Pennycook SJ, Anderson IM, Minor AM, Schmid AK, Duden T, Radmilovic V, Ramasse QM, Watanabe M, Erni R, Stach EA, Denes P & Dahmen U (2008). Detection of single atoms and buried defects in three dimensions by aberration-corrected electron microscope with 0.5-Å information limit. *Microsc Microanal* **14**, 469–477.
- Lehmann S, Wallentin J, Jacobsson D, Deppert K & Dick KA (2013). A general approach for sharp crystal phase switching in InAs, GaAs, InP, and GaP nanowires using only group V flow. *Nano Lett* **13**, 4099–4105. doi:10.1021/nl401554w
- Lenrick F, Ek M, Deppert K, Samuelson L & Reine Wallenberg L (2014). Straight and kinked InAs nanowire growth observed in situ by transmission electron microscopy. *Nano Res* **7**, 1188–1194.
- Maliakkal CB, Jacobsson D, Tornberg M, Persson AR, Johansson J, Wallenberg R & Dick KA (2019). In situ analysis of catalyst composition during gold catalyzed GaAs nanowire growth. *Nat Commun* **10**, 4577. doi:10.1038/s41467-019-12437-6
- Mirsaidov U, Patterson JP & Zheng H (2020). Liquid phase transmission electron microscopy for imaging of nanoscale processes in solution. *MRS Bull* **45**, 704–712.
- Oh SH, Kauffmann Y, Scheu C, Kaplan WD & Rühle M (2005). Ordered liquid aluminum at the interface with sapphire. *Science (New York, NY)* **310**, 661–663.
- Omme JTV, Zakhosheva M, Spruit RG, Sholkina M & Pérez HH (2018). Ultramicroscopy advanced microheater for in situ transmission electron microscopy: Enabling unexplored analytical studies and extreme spatial stability. *Ultramicroscopy* **192**, 14–20. doi:10.1016/j.ultramic.2018.05.005
- Persson AR, Tornberg M, Sjökvist R & Jacobsson D (2021). Time-resolved compositional mapping during in situ TEM studies. *Ultramicroscopy* **222**, 113193. doi:10.1016/j.ultramic.2020.113193
- Prestat E, Smith M, Janssen A, Slater TJA, Camargo PHC, Kulzick MA, Grace Burke M, Haigh SJ & Zaluzec NJ (2015). XEDS and EELS in the TEM at atmospheric pressure and high temperature. *Microsc Microanal* **21**, 247–248. doi:10.1017/S1431927615002032
- Ross FM, Tersoff J, Reuter M, LeGoues FK & Tromp RM (1998). In situ transmission electron microscopy observations of the formation of self-assembled Ge islands on Si. *Microsc Res Tech* **42**, 281.
- Straubinger R, Beyer A, Ochs T, Stolz W & Volz K (2017). In situ thermal annealing transmission electron microscopy (TEM) investigation of III/V semiconductor heterostructures using a setup for safe usage of toxic and pyrophoric gases. *Microsc Microanal* **23**, 751–757.
- Tan SF, Chee SW, Baraisov Z, Jin H, Tan TL & Mirsaidov U (2019). Real-time imaging of nanoscale redox reactions over bimetallic nanoparticles. *Adv Funct Mater* **29**, 1–10.
- Tornberg M, Maliakkal CB, Jacobsson D, Dick KA & Johansson J (2020). Limits of III-V nanowire growth based on droplet dynamics. *J Phys Chem Lett* **11**, 2949–2954.
- Toth P, Jacobsson D, Ek M & Wiinikka H (2019). Real-time, in situ, atomic scale observation of soot oxidation. *Carbon* **145**, 149–160.
- Wang N, Yuan X, Zhang X, Gao Q, Zhao B, Li L, Lockrey M, Tan HH, Jagadish C & Caroff P (2019). Shape engineering of InP nanostructures by selective area epitaxy. *ACS Nano* **13**, 7261.